This manuscript has been accepted for publication in *Journal of Geophysical Research: Solid Earth.*
https://doi.org/10.1029/2020JB021077

# High-Pressure Deformation of Iron–Nickel–Silicon Alloys and Implications for Earth's Inner Core

**Matthew C. Brennan[1], Rebecca A. Fischer[1], Samantha Couper[2], Lowell Miyagi[2], Daniele Antonangeli[3], Guillaume Morard[3,4]**

[1]Department of Earth and Planetary Sciences, Harvard University

[2]Department of Geology and Geophysics, University of Utah

[3]Sorbonne Université; Muséum National d'Histoire Naturelle; UMR CNRS 7590; Institut de Minéralogie, de Physique des Matériaux et de Cosmochimie; IMPMC

[4]Université Grenoble Alpes; Université Savoie Mont Blanc; CNRS; IRD; Université Gustave Eiffel; ISTerre

Corresponding author: Matthew C. Brennan (mcbrennan@g.harvard.edu)

## Key Points:

- The inner core's seismic anisotropy can be explained by crystallographic alignment of a hexagonal close-packed iron-rich alloy.
- Sample textures suggest that silicon-bearing alloy deformation may be dominated by pyramidal and basal slip at low and high *T*, respectively.
- Silicon-bearing alloys are stronger (harder to deform) at inner core conditions than pure iron and iron–nickel alloys.

## Abstract

Earth's inner core exhibits strong seismic anisotropy, often attributed to the alignment of hexagonal close-packed iron (hcp-Fe) alloy crystallites with the Earth's poles. How this alignment developed depends on material properties of the alloy and is important to our understanding of the core's crystallization history and active geodynamical forcing. Previous studies suggested that hcp-Fe is weak under deep Earth conditions but did not investigate the effects of the lighter elements known to be part of the inner core alloy. Here, we present results from radial X-ray diffraction experiments in a diamond anvil cell that constrain the strength and deformation properties of iron–nickel–silicon (Fe–Ni–Si) alloys up to 60 GPa. We also show the results of laser heating to 1650 K to evaluate the effect of temperature. Observed alloy textures suggest different relative activities of the various hcp deformation mechanisms compared to pure Fe, but these textures could still account for the theorized polar alignment. Fe–Ni–Si alloys are mechanically stronger than Fe and Fe–Ni; extrapolated to inner core conditions, Si-bearing alloys may be more than an order of magnitude stronger. This enhanced strength proportionally reduces the effectivity of dislocation creep as a deformation mechanism, which may suggest that texture developed during crystallization rather than as the result of post-solidification plastic flow.

## Plain Language Summary

The inner core is a Moon-sized ball of solid metal at the very center of the Earth. Vibrations from earthquakes move faster through the inner core if they travel parallel to Earth's axis (the line between the North and South Poles) than if they travel parallel to the Equator. This probably means that the grains of metal in the inner core are themselves aligned with Earth's axis. Previous studies determined that this alignment likely happened after the inner core had formed, but those experiments were done on pure iron, whereas the inner core is mostly iron but also contains other elements. We did experiments at high pressures and temperatures on a more realistic core metal containing iron, nickel, and silicon. We found that this metal would be much stronger than pure iron at inner core pressures and temperatures; it is still possible for it to produce a north–south alignment, but it is much more difficult for it to do so. This could mean that the alignment occurred while the inner core was forming (rather than afterward), which might change how we think about the forces present in the deep Earth today.

## 1 Introduction

Since the discovery of the inner core (Lehmann, 1936) and its identification as a solid iron alloy (Birch, 1952), seismic studies have revealed it to be complexly structured and seismically anisotropic. On average, seismic waves move through the inner core several percent faster on paths parallel to Earth's axis of rotation compared to perpendicular paths (e.g., Deuss, 2014). This anisotropy is well documented by travel time (e.g., Creager, 1992) and normal mode (e.g., Durek & Romanowicz, 1999) observations, and deviations from this large-scale anisotropy have been used to suggest other inner core structural features (e.g., Irving & Deuss, 2011; Ishii & Dziewoński, 2002; Ouzounis & Creager, 2001; Su & Dziewoński, 1995). These secondary structures are frequently invoked as evidence for various proposed mechanisms of the primary anisotropy's development.

As with many instances of seismic anisotropy, the Earth's inner core structure likely arises from preferred orientation of crystallites (i.e., texture). Solid Fe-rich alloys (including those in the Fe–Ni–Si system) are expected to exist in the hexagonal close-packed (hcp) crystal structure (ε-Fe) at inner core pressures (*P*) and temperatures (*T*) (e.g., Sakai et al., 2011; Tateno et al., 2010, 2012, 2015). Since hcp crystals are seismically fast parallel to their *c*-axes (Bergman et al., 2000), a preferential alignment of the inner core's crystals with Earth's axis of rotation is widely accepted as responsible for the inner core anisotropy (e.g., Antonangeli et al., 2006; Sakai et al., 2011; Sayers, 1989; Stixrude & Cohen, 1995; Vočadlo et al., 2009). This explanation is experimentally supported by observations of strong *c*-axis aligned deformation textures in hcp metals, including ε-Fe (e.g., Antonangeli et al., 2006; Merkel et al., 2012, 2013; Miyagi et al., 2008; Wenk et al., 2000). It is worth noting that cubic Fe polymorphs cannot deform to produce a texture compatible with the observed anisotropy (Lincot et al., 2016).

There is considerable diversity amongst the mechanisms proposed to create this texture. One class of models relies on preferred orientation developing during crystallization (e.g., Karato, 1993; Bergman, 1997). However, if crystals instead solidify in random orientations, texture must develop by plastic flow in the solid aggregate. This can result from solid-state convection (e.g., Buffett, 2009; Deguen et al., 2013; Jeanloz & Wenk, 1988) or from west-to-east translation due to preferential solidification in one hemisphere (e.g., Alboussiere et al., 2010; Bergman et al., 2010; Monnereau et al., 2010). Flow may also be driven by forces external to the inner core, such as electromagnetism (e.g., Buffet & Wenk, 2001; Takehiro, 2011) or outer core convection (e.g., Aubert et al., 2008; Yoshida et al., 1996). Experimentally, Gleason & Mao (2013) found that Fe is very weak at ultra-high pressures. If this holds true for the inner core, post-solidification texturing could be driven by almost any source of differential stress, making it difficult to discriminate between various models.

An important caveat of previous studies is that they have investigated pure ε-Fe, but the core is known to also contain other elements. Ni is expected to be present at approximately 5 weight percent (wt%) (e.g., McDonough & Sun, 1995), but Fe–Ni is too dense and seismically fast to account for core properties, so a much lighter element must also be present (Birch, 1964). The identity of the light element(s) is one of the most controversial problems in deep Earth geophysics, but Si is a leading contender based on its ability to partition into the metallic phase during core formation (e.g., Fischer et al., 2015; Siebert et al., 2013) and the isotopic (Georg et al., 2007) and major-element (Ringwood, 1961) ratios of terrestrial rocks. Estimates of inner core Si based on density range as high as 7 wt% (Fischer et al., 2014; Tateno et al., 2015), but this should be considered an upper bound since Si is unlikely to be the sole alloying light element (e.g., Edmund et al., 2019; Ozawa et al., 2016).

The presence of alloying elements may alter the deformation mechanisms and resultant texture of the inner core. Metallurgical studies have demonstrated that Ni (e.g., Ledbetter & Reed, 1973) and Si (e.g., Ros-Yanez et al., 2007) can significantly alter the mechanical properties of Fe. A previous experimental study (Reagan et al., 2018) on Fe–Ni alloys at high pressure did not characterize textures but found that addition of 5.5 wt% Ni could increase the strength (defined as the shear stress needed to induce plastic deformation) of Fe by 25% at inner core conditions. This increase alone is unlikely to change the dominant mechanism of inner core texturing, but a light element, possibly combined with strain hardening (Bergman et al., 2014), could further strengthen the alloy. Geodynamical models have difficulty reproducing seismic observations by imposing plausible flows on ε-Fe (Lasbleis & Deguen, 2015; Lincot et al., 2014), but this issue may disappear if alloy deformation textures are distinct from those of pure Fe. In this study, we measure both the strength and texture of deformed Fe–Ni–Si alloys to determine whether an alloying light element significantly changes the mode of plastic deformation or the interpreted strength of the inner core.

## 2 Methods

We investigated the properties of five Fe–Ni–Si alloys: Fe–9wt% Si (hereafter Fe–9Si) was a powder (Goodfellow FE166014); Fe–6Ni–8Si was synthesized in a piston-cylinder press at Harvard University (composition checked by energy dispersive spectroscopy); and Fe–5Si, Fe–5Ni–5Si, and Fe–5Ni–10Si were synthesized as foils by ultra-rapid quenching at the Institut de Chimie et des Matériaux de Paris-Est (details in Morard et al., 2011). Non-foil samples were loaded as powders and foil samples were laser-drilled into cylindrical slugs. All samples filled the sample chambers, which were 50 µm diameter cylindrical holes drilled into amorphous boron gaskets contained in Kapton supporting rings. This configuration allows X-rays to pass radially through the gasket and sample (Merkel & Yagi, 2005). A Pt flake was loaded along with each sample as a pressure standard (Fei et al., 2007). Samples were compressed between diamonds with 200 µm diameter culets in panoramic piston-cylinder type diamond anvil cells to initial pressures of 2–3 GPa. Additional compression was accomplished by an inflating gas membrane once the cell was on the beamline. We repeated the Fe–5Si experiment with double-sided laser heating during compression. For that experiment, gaskets were laser drilled from cubic boron nitride, and MgO flakes were used as thermal insulators and pressure standards (Speziale et al., 2001).

Experiments were conducted at Advanced Light Source beamline 12.2.2 ($\lambda = 0.4613$ or 0.4592 Å) with the diamond anvil cell mounted with its compression axis orthogonal to the X-ray beam (Kunz et al., 2005). The detector was a mar345 positioned 385 or 386 mm from the sample, and the calibrant was $CeO_2$ at ambient conditions. For each pressure step, a diffraction pattern was collected with a 120 second exposure. We used the program Dioptas (Prescher & Prakapenka, 2015) for live pattern integration, which allowed us to monitor phase changes and sample pressure during the experiment. Diffraction patterns were collected as the samples were compressed gradually to 50–60 GPa, near the maximum stability of the boron gaskets (Merkel & Yagi, 2005). Membrane pressure was then released over several hours while simultaneously collecting decompression patterns. Diffraction data were analyzed via Rietveld refinement (McCusker et al., 1999) in the crystallographic software package MAUD (Lutterotti et al., 1999). We analyzed several diffraction patterns for each experiment, including at least one pattern in the body-centered cubic (bcc) and the bcc–hcp transition regions, and at least four in the hcp region. Patterns were chosen based on their diffraction intensity, possession of sufficient Pt diffraction to refine an accurate pressure, and equally spaced coverage of the experiment's pressure range. These patterns were refined over a $2\theta$ range of 11.5–25°and refined unit cell dimensions and elastic strains were compiled for the hcp phase of each sample (Supporting Information Table S1). Textures were calculated using the Extended Williams-Imhof-Matthies-Vinel (E-WIMV) model (Chateigner et al., 2019) with fiber symmetry imposed about the axis of compression. Orientation density functions were refined at a resolution of 15°, exported to BEARTEX (Wenk et al., 1998), and smoothed with a 10° Gaussian filter prior to plotting as inverse pole figures (Section 3). The pressures of phase transitions in 300 K samples may not necessarily be the same as at equilibrium due to sluggish kinetics, starting material effects, and non-hydrostaticity, but the measured texture and strength of the phases present are still accurate.

## 3 Deformation Textures

As in pure Fe, our alloy samples transformed from the bcc (or bcc-like: Fischer et al., 2013) structure to the hcp structure upon compression. The deformation textures of our room-temperature experiments are shown in Figure 1. The bcc textures are near-identical to those of pure Fe (e.g., Merkel et al., 2004; Miyagi et al., 2008), varying only in the strength of the $100$ maximum. The similarity across compositions suggests that sufficient plastic flow occurred prior to the bcc–hcp transition to homogenize the textures (except for possibly in Fe–9Si, which may have led to its distinctive hcp texture). Once the transition to hcp is complete, the alloy textures show two distinct maxima: one near $11\bar{2}0$ and one near $0001$. The non-foil samples (Fe–9Si and Fe–6Ni–8Si) are distinguished by the absence of the latter maximum; these were mechanically strong (Section 4) but weakly textured, perhaps indicating that plastic flow was impeded in these experiments. The non-foil textures are likely the result of compressive $\{2\bar{1}\bar{1}2\}\langle 2\bar{1}\bar{1}3\rangle$ twinning. This deformation mechanism is known to occur at large strains and low temperatures in ε-Fe (Kanitpanyacharoen et al., 2012; Merkel et al., 2004), so its presence at 300 K in our strongest alloys is reasonable. The foil experiments were more strongly textured (showing strong maxima at $11\bar{2}0$ and $0001$), so they may be better representatives of texture development by dislocations (the type of deformation texturing proposed to occur in the inner core, see Section 4.4). Polycrystal plasticity simulations of hcp metals (e.g., Chapuis & Liu, 2015; Kanitpanyacharoen et al., 2012; Miyagi et al., 2008; Wenk et al., 2000) have shown that basal $(0001)\langle 2\bar{1}\bar{1}0\rangle$ slip produces the $0001$ maximum, while pyramidal $\{2\bar{1}\bar{1}2\}\langle 2\bar{1}\bar{1}3\rangle$ slip produces the $11\bar{2}0$ maximum. A large pyramidal contribution can result in a ~30° shift in the $0001$ maximum (Miyagi et al., 2008; Merkel et al., 2013), as is seen in the Fe–5Ni–10Si textures. Together, these foil textures show evidence of significant pyramidal slip. Since basal slip is typically observed to dominate ε-Fe deformation at 300 K (e.g., Nishihara et al., 2018) we surmise that addition of Si increases the activity of pyramidal slip. Prismatic $\{10\bar{1}0\}\langle\bar{1}2\bar{1}0\rangle$ slip is also likely to be active without producing a distinct textural signature (Merkel et al., 2004).

**Figure 1.**

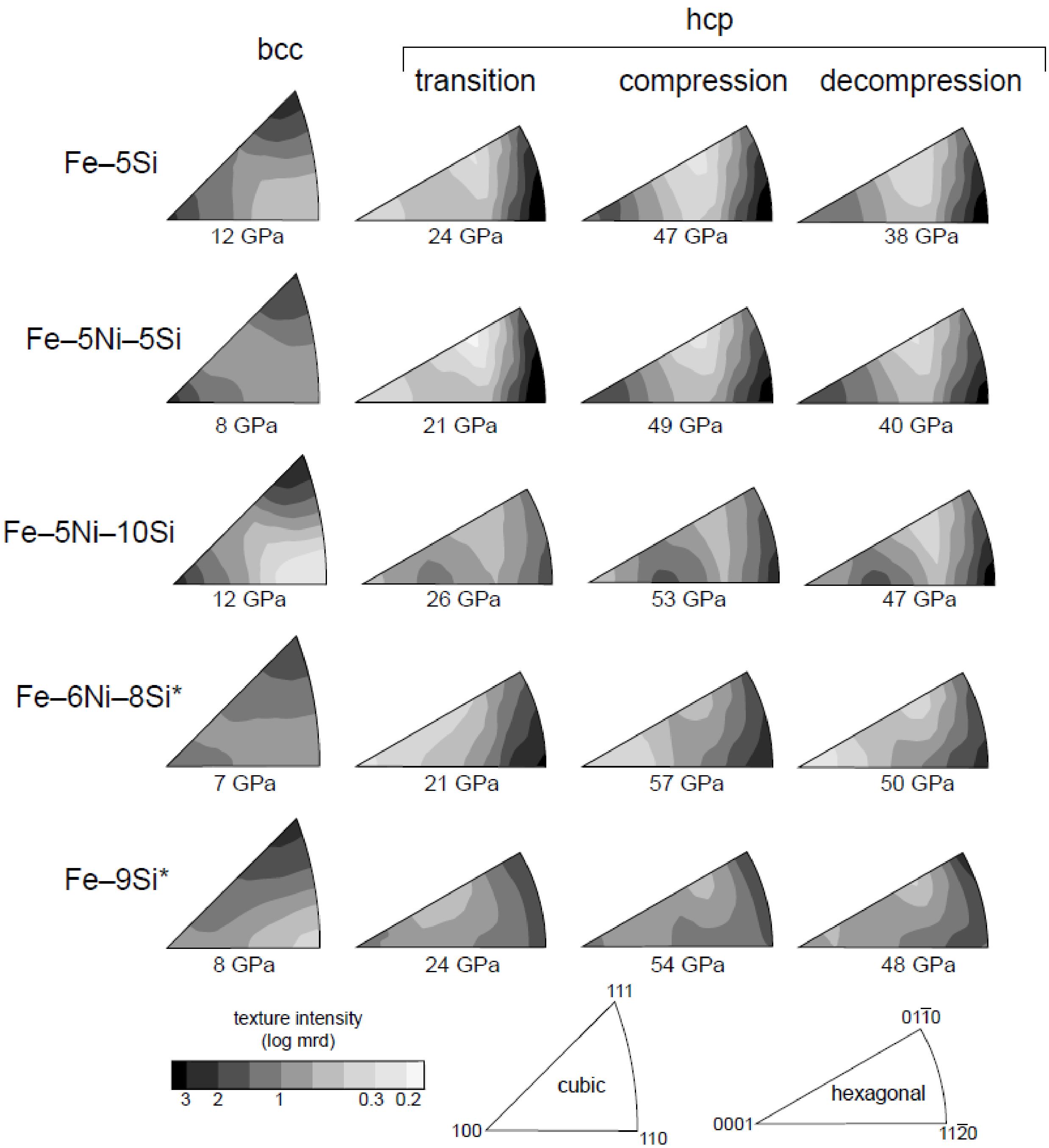

Inverse pole figures (IPFs) showing alloy deformation textures at room temperature. The bcc textures were collected before the appearance of hcp, "transition" textures were collected in the bcc–hcp coexistence region, "compression" textures were collected during compression near peak sample pressure (in the hcp-only regime), and "decompression" textures were collected after the sample had relaxed by 5–10 GPa. Textural differences appear upon transformation to hcp and become more pronounced upon compression. Sample textures remained consistent upon decompression, in contrast to Miyagi et al. (2008). Asterisks indicate non-foil starting materials (Section 2). All IPFs are plotted on the same intensity scale, quantified as multiples of randomly distributed crystallographic orientations (mrd). Typical pressure uncertainties are ~5%.

Laser-heated deformation textures of a different Fe–5Si experiment are shown in Figure 2. Compared to the 300 K data, the high-temperature textures show a basal slip maximum focused in the $0001$ direction and much stronger in intensity than the pyramidal maximum at $11\bar{2}0$. Consistent with the phase relations reported by Komabayashi et al. (2019), a few face-centered cubic (fcc) grains (< 2 volume % from the Rietveld refinement) crystalized above 1400 K (Supporting Information Figure S3), but they are likely too scarce to have influenced the texture; Miyagi et al. (2008) did not observe hcp textural changes even at higher fcc abundances. Focused $0001$ textures previously observed in pure Fe have been attributed to basal slip (Nishihara et al., 2018; Wenk et al., 2000) and tensile twinning (Merkel et al., 2012). Since heating disrupts twinning mechanisms, and there is no textural evidence for strong pyramidal slip (unlike at 300 K), it seems that deformation at high temperatures favors basal slip. This effect was previously suggested for ε-Fe by Steinle-Neumann et al. (2001) and could be associated with the high temperature breakdown of $\langle c + a \rangle$ deformation mechanisms observed in other hcp metals (Fan et al., 2017; Poirier & Langenhorst, 2002).

**Figure 2.**

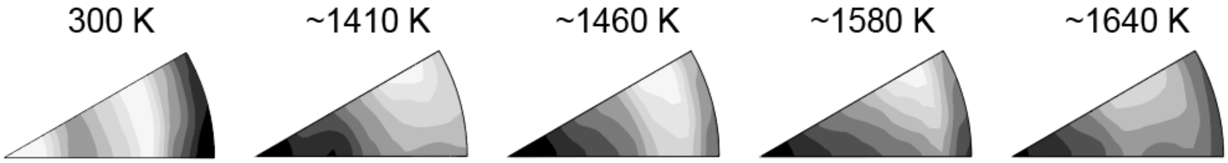

IPFs of the hcp phase from diffraction images taken in the laser-heated Fe–5Si experiment. The 300 K pole figure was collected at 24 GPa (prior to any laser heating), and the others were taken consecutively during a cycle of simultaneous heating and compression at 43–46 GPa. The basal slip maximum at high temperatures is stronger and more focused on $0001$ compared to 300 K textures, while a weaker local maximum appears to persist at $11\bar{2}0$, suggesting continued pyramidal slip activity. This texture persisted upon temperature quenching. Geometries and intensity scales are the same as in Figure 1. Typical temperature uncertainties are ~10%.

The relative dominance of basal and pyramidal slip systems may be significant to our understanding of the inner core. As mentioned above, most studies predict basal slip to dominate ε-Fe deformation at deep-Earth conditions since this mechanism produces strong $0001$ textures analogous to the observed polar anisotropy (e.g., Wenk et al., 2000). We see this same texture in our heated experiment, so we cannot rule out this interpretation. However, some studies (e.g., Lincot et al., 2016; Steinle-Neumann et al., 2001) have suggested that pyramidal slip may be required to match seismic observations. In that case, our finding of significant pyramidal activity in Si-bearing alloys may help explain the discrepancy between the observed and expected modes of plastic deformation. Of course, it is also possible that the inner core texture is a solidification product and was not created by plastic deformation at all (Section 4.4).

## 4 Alloy Strength

Our experiments allow us to measure elastic stress in the sample and quantify its dependence on pressure and temperature. Calculating mechanical strength also requires knowledge of the alloys' shear moduli, the values of which were taken from previous studies. We extrapolate these parameters to inner core conditions to compare the mechanical strength implied by our Si-bearing experiments to previously-published estimates for Fe and Fe–Ni.

### 4.1 Strength calculations

The yield strength of a material is defined by the boundary between stresses low enough to be supported elastically and stresses high enough to induce plastic deformation (i.e., flow). In our experiments, the elastic stress resolved on a specific diffraction peak is determined by the dimensionless parameter $Q(h\ k\ l)$, where $h$, $k$, and $l$ are the Miller indices of the peak. This parameter is related to deviatoric (i.e., differential) stress by:

$$Q(h\ k\ l) = \frac{t}{3}\left[\frac{\alpha}{2G_R(h\ k\ l)} + \frac{(1-\alpha)}{2G_V}\right] \tag{1}$$

where $G_V$ is the Voight approximation shear modulus, $G_R(h\ k\ l)$ is the Reuss approximation shear modulus of the peak (Anderson, 1965), α is a weighting factor, and $t$ is the deviatoric stress:

$$t = \sigma_1 - \sigma_3 \tag{2}$$

where $\sigma_1$ and $\sigma_3$ are the maximum and minimum stress components, respectively (Singh et al., 1998). Calculating $G_R(h\ k\ l)$ requires single-crystal compliance moduli ($S_{ij}$) for the sample material under conditions of hydrostatic pressure. Since these are seldom available, it is common to assume $G_R(h\ k\ l) = G_V = G$, where $G$ is the aggregate shear modulus, a measurable quantity. These assumptions reduce Equation 1 to:

$$t = 6G\langle Q(h\ k\ l)\rangle \tag{3}$$

where $\langle Q(h\ k\ l)\rangle$ (hereafter $Q$) is an average across all observed peaks in a diffraction pattern. If the sample's yield strength has been exceeded and it is plastically flowing, elastic deformation cannot accommodate any more strain, the peaks are expressing their maximum possible $Q$, and $t$ is equal to the material's yield strength (Hemley et al., 1997). Determining alloy strengths at conditions relevant to the inner core requires extrapolating both $G$ and $Q$ to high pressures (>330 GPa) and temperatures (>3000 K).

### 4.2 Extrapolation of $Q$

The pressure dependence of $Q$ in our experiments is shown in Figure 3. Each experiment shows a positive linear relationship between $P$ and $Q$, with four of the five experiments having similar slopes and Fe–5Ni–5Si exhibiting a shallower pressure dependence. There are no apparent experimental reasons for this deviation; Fe–5Ni–5Si is intermediate among the sample compositions, did not have large uncertainties in $Q$, had the same dimensions as the other samples, and the other two foil experiments did not exhibit shallow slopes. Extrapolating each trend to inner core pressures (Figure 3 inset) results in indistinguishable values for each experiment except Fe–5Ni–5Si. Since there does not appear to be a compositional trend in $Q$ values, and we cannot rule out the shallower $\partial Q/\partial P$, the following analysis will present results using both a fit to all the experimental alloys ($\partial Q/\partial P = (1.1 \pm 0.1) \times 10^{-4}\ \mathrm{GPa}^{-1}$) and a fit to only Fe–5Ni–5Si ($\partial Q/\partial P = (4.4 \pm 0.9) \times 10^{-5}\ \mathrm{GPa}^{-1}$). Both fits are steeper than literature values for Si-free alloys. For example, the highest value found by Regan et al. (2018) was $\partial Q/\partial P \approx 3 \times 10^{-5}\ \mathrm{GPa}^{-1}$ for Fe–20Ni.

**Figure 3.**

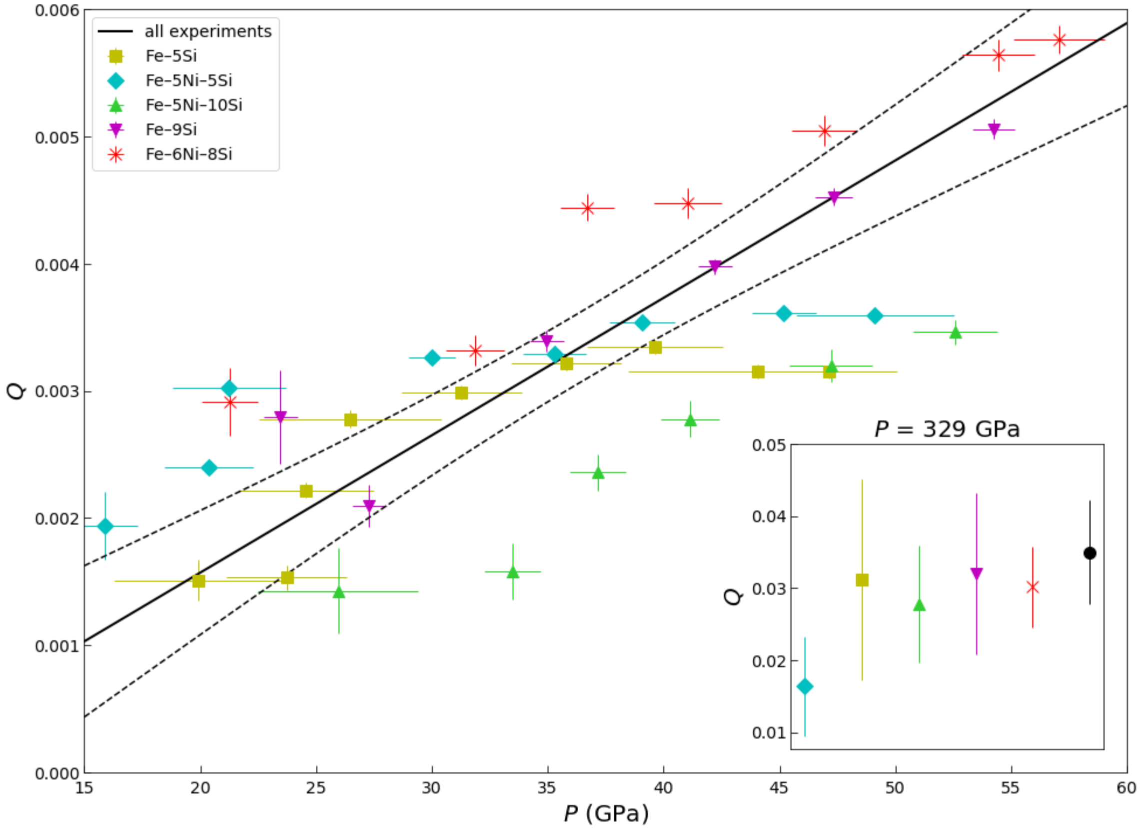

Pressure evolution of $\langle Q(h\,k\,l)\rangle$ for the hcp phase of each composition at 300 K. Relative strengths between the alloys do not appear to show significant compositional dependence, even within the three experiments (Fe–5Si, Fe–5Ni–5Si, Fe–5Ni–10Si) synthesized as foils. All these data were collected on compression. Fits to $\partial Q/\partial P$ for each composition (not shown) and to all data (solid line; dashed lines are 95% confidence intervals) were calculated by orthogonal distance regression considering the error bars of each point. **Inset:** These fits (and 95% confidence intervals) extrapolated to 329 GPa, the inner core boundary pressure. At this pressure, Fe–5Ni–5Si is noticeably weaker than the other alloys.

Our laser-heated Fe–5Si experiment allows us to estimate the effect of temperature on $Q$. As expected, high temperatures enhance plastic deformation, reducing the elastically-supported strain and resulting in $Q$ reduction at a rate of $\partial Q/\partial T = (-1.60 \pm 0.36) \times 10^{-6}\ \mathrm{K}^{-1}$ (Supporting Information Figure S1). There are significant experimental limitations to this technique; the minimum power threshold for laser emission prevents measurements at intermediate temperatures, and laser heating generates large temperature gradients in the sample. However, Merkel et al. (2013) constrained the temperature effect on pure Fe by compiling data from several resistively-heated diamond anvil cell and multi-anvil experiments, and their reported alloy strengths imply $\partial Q/\partial T$ consistent with our value for reasonable (i.e., H. Mao et al., 1999) values of *G* (Equation 3). Previous studies that extrapolated experimental values to inner core conditions (Gleason & Mao, 2013; Regan et al., 2018) assumed ${\partial Q}/_{\partial T} = 0\ \mathrm{K}^{-1}$, meaning their calculated inner core strengths were upper bounds. In the following analysis, we recalculate their results using our estimated ${\partial Q}/_{\partial T}$ value.

### 4.3 Extrapolation of *G*

In addition to *Q*, it is necessary to extrapolate shear modulus *G* to core-relevant conditions (Equation 3). Although Dubrovinsky et al. (2000) describes a technique to determine *G* values by Rietveld refinement, this requires high-quality and quasi-hydrostatic diffraction, restrictions incompatible with radial geometry experiments. Relatively few studies report shear modulus values, but from the relationships

$$V_S = \sqrt{\frac{G}{\rho}} \tag{4}$$

$$V_P = \sqrt{\frac{K+\frac{4}{3}G}{\rho}} \tag{5}$$

(where $V_S$ is shear velocity, $V_P$ is compressional velocity, ρ is density, and *K* is bulk modulus), *G* can be extracted from simultaneous density and velocity measurements. Figure 4 shows *G* versus *P* for available experimental data from the literature on Si-bearing hcp alloys. There is a clear difference between experimental techniques, with nuclear-resonant inelastic X-ray scattering (NRIXS) studies finding systematically lower *G* values than inelastic X-ray scattering (IXS) or acoustic methods. We will use NRIXS values for the following calculations since experimental uncertainties are sufficient to make extrapolated results of the techniques overlap at inner core conditions (Figure 4 inset). Note that while a linear *G* versus *P* relationship is experimentally supported at least to 220 GPa (H. Mao et al., 1999), a sublinear relationship could potentially reduce the shear modulus at inner core conditions.

Following the method of previous high-pressure strength studies (Gleason & Mao, 2013; Reagan et al., 2018), we extrapolated *G* using the formalism of Steinburg et al. (1980):

$$G(P,T) = G_0 + \frac{\partial G}{\partial P}\frac{P}{\left({}^{\rho}/_{\rho_0}\right)^{1/3}} + \frac{\partial G}{\partial T}(T-300) \tag{6}$$

where subscript 0 indicates ambient conditions (*T* = 300 K, *P* = 1 bar) and ρ is molar density. Values of $G_0$ and ${\partial G}/_{\partial P}$ are taken from the NRIXS fit in Figure 4, $\rho_0$ is from equation of state literature (Fe–5Si from Edmund et al., 2019; Fe–5Ni–5Si from Edmund et al., 2020; other alloys calculated from these and the pure Fe values of Dewaele et al., 2006), ρ is the PREM inner core density, and *G*(*P*,*T*) is calculated from ρ and the PREM inner core shear velocity (Dziewonski & Anderson, 1981). Selecting locations in the inner core, namely the inner core boundary (ICB) and inner core center (ICC), allows ${\partial G}/_{\partial T}$ to be solved at the corresponding pressure and temperature conditions. This calculation implicitly assumes that the inner core has the same composition as the material used to derive the other parameters, which is most reasonable for compositions with Ni and Si. The calculation is also subject to the large (but difficult to quantify) uncertainty on the temperature of the inner core (e.g., Karato, 2008). Considering this, we elected to use the same inner core temperatures as Gleason & Mao (2013) and Reagan et al. (2018) (5500 K at the ICB, 6200 K at the ICC) to ensure that our results are directly comparable to their

Si-free results; the differences between studies are not dependent on the specific pressure and temperature conditions. Calculated $\partial G/_{\partial T}$ values vary little between compositions; average values are –0.050 ± 0.008 GPa $K^{-1}$ at the ICB and –0.043 ± 0.006 GPa $K^{-1}$ at the ICC. These values are smaller than the corresponding values of Fe–12Ni (Reagan et al., 2018) and Fe (Gleason & Mao, 2013) by a factor of 1.25 and a factor of 2 respectively because of our smaller $\partial G/_{\partial P}$ term.

**Figure 4.**

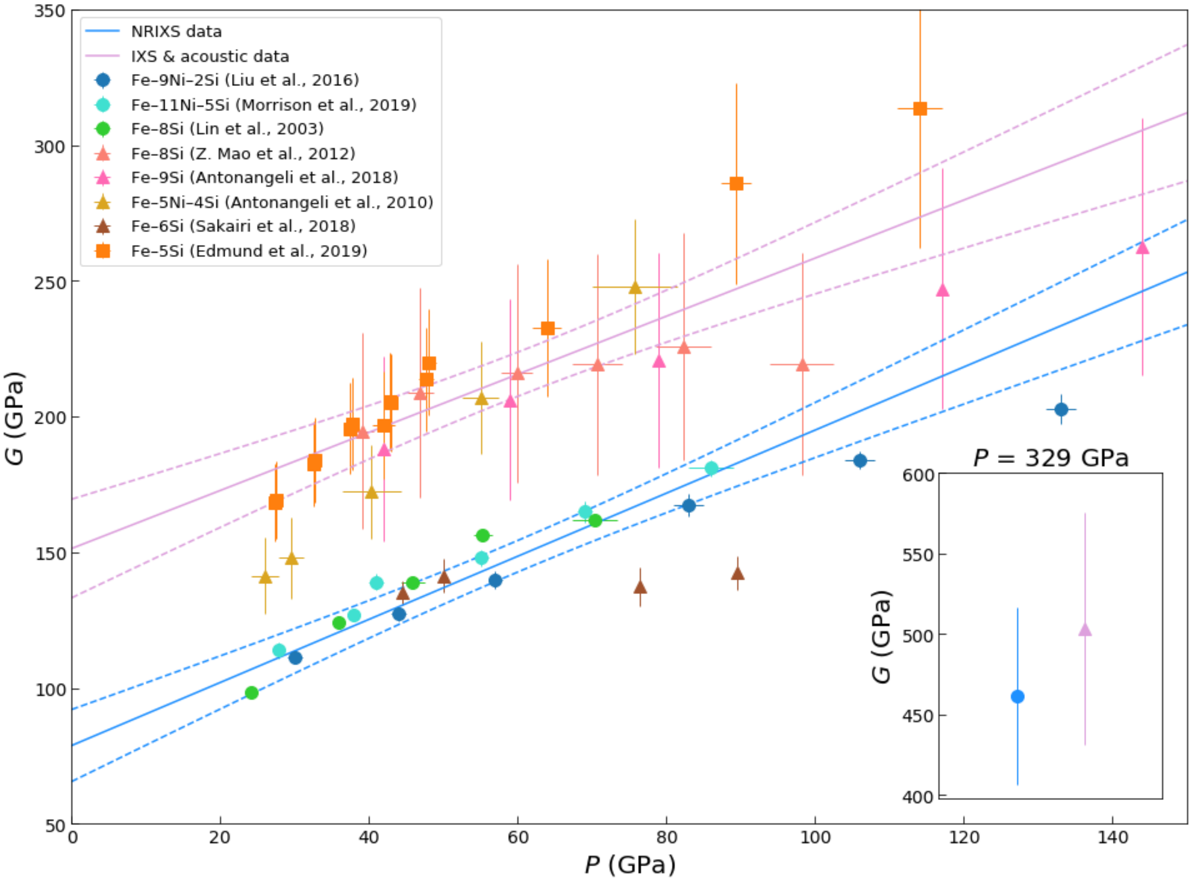

Published experimental values of the shear moduli of hcp alloys in the Fe–Si and Fe–Ni–Si systems at 300 K, either explicitly reported or implied (Equations 4 and 5). The pink line is a fit to data collected by IXS and picosecond acoustic techniques (triangles and squares, respectively), excluding Sakairi et al. (2018). The blue line is a fit to NRIXS data (circles) and is corrected for $^{57}$Fe enrichment. For context, a fit to experimental measurements of pure hcp-Fe would plot about halfway between these lines (e.g., H. Mao et al., 1999). Both fits (solid lines) are calculated irrespective of composition by orthogonal distance regression and are shown with 95% confidence intervals (dashed lines). **Inset:** These fits (and confidence intervals) extrapolated to 329 GPa. At this pressure, the techniques are indistinguishable within error.

### 4.4 Predicted inner core strength

Calculated alloy strength as a function of temperature is shown in Figure 5. Merkel et al. (2013) calculated trends directly as a function of *t* (rather than treating *G* and *Q* individually) based on several data spanning different studies and techniques. Extrapolating, their results imply stronger Fe than Gleason & Mao (2013) but still consistently weaker than our Si-bearing values. Even the Fe–5Ni–5Si experiment (with shallower $\partial Q/_{\partial P}$) is stronger than all Si-free compositions. If solid state deformation occurs in the inner core, this enhanced strength may influence our interpretation of whether deformation is dominated by the flow of atoms towards concentrations of vacancy defects (diffusion creep) or the movement of lattice dislocations (power-law creep). Van Orman (2004) suggested the additional possibility of dislocation flow via "Harper-Dorn creep", but this mechanism is controversial (e.g., Kassner et al., 2015). Adjudicating between mechanisms is important because diffusion creep typically does not produce lattice-preferred orientation and thus would not generate anisotropy. Therefore, if the inner core is in a diffusion-dominated regime, this would tend to support anisotropy developing during crystallization rather than afterwards.

Gleason & Mao (2013) concluded that their pure Fe data were consistent with dislocation-dominated (power-law) creep since mechanical weakness enhances dislocation mobility, allowing geophysically-plausible stresses to produce the required strain rates. Figure 6 (panels a and b) compares their results to those of Reagan et al. (2018) and this study. For a given differential stress, dislocation velocities and strain rates are about one order of magnitude reduced for Si-bearing alloys compared to pure Fe. An approximately equal depression is obtained (for both velocity and strain rate) by moving from the ICB to the ICC for a given alloy. Figure 6c shows a calculation of the boundary between diffusion- and dislocation-dominated regimes based on the parametrization of Reaman et al. (2011), which depends on $G(P,T)$ and $\rho$, but not explicitly on $t$. Here, the depressed $G$ values of Si-bearing alloys slightly enlarge the dislocation-dominated field. It is important to note that our knowledge of inner core properties is incomplete. Estimates of the inner core stress field ($\tau$) span at least five orders of magnitude (Buffet & Wenk, 2001; Koot & Dumberry, 2011; Yoshida et al., 1996). Likewise, estimates of the inner core's grain size vary widely, with constraints from earlier studies (e.g., Bergman, 1998) permitting crystallites as small as several centimeters while more recent studies (e.g., Yamazaki et al., 2017) prefer much larger grain sizes. These uncertainties make it impossible to say definitively which field the inner core falls in. Additionally, inner core viscosity, itself a poorly constrained parameter, determines the relationship between applied stress and strain rate. Gleason & Mao (2013) suggested a viscosity range of $10^{15}$–$10^{19}$ Pa s assuming a pure Fe inner core and simple isotropic shear; our "all alloys" fit would be one order of magnitude more viscous under the same conditions.

**Figure 5.**

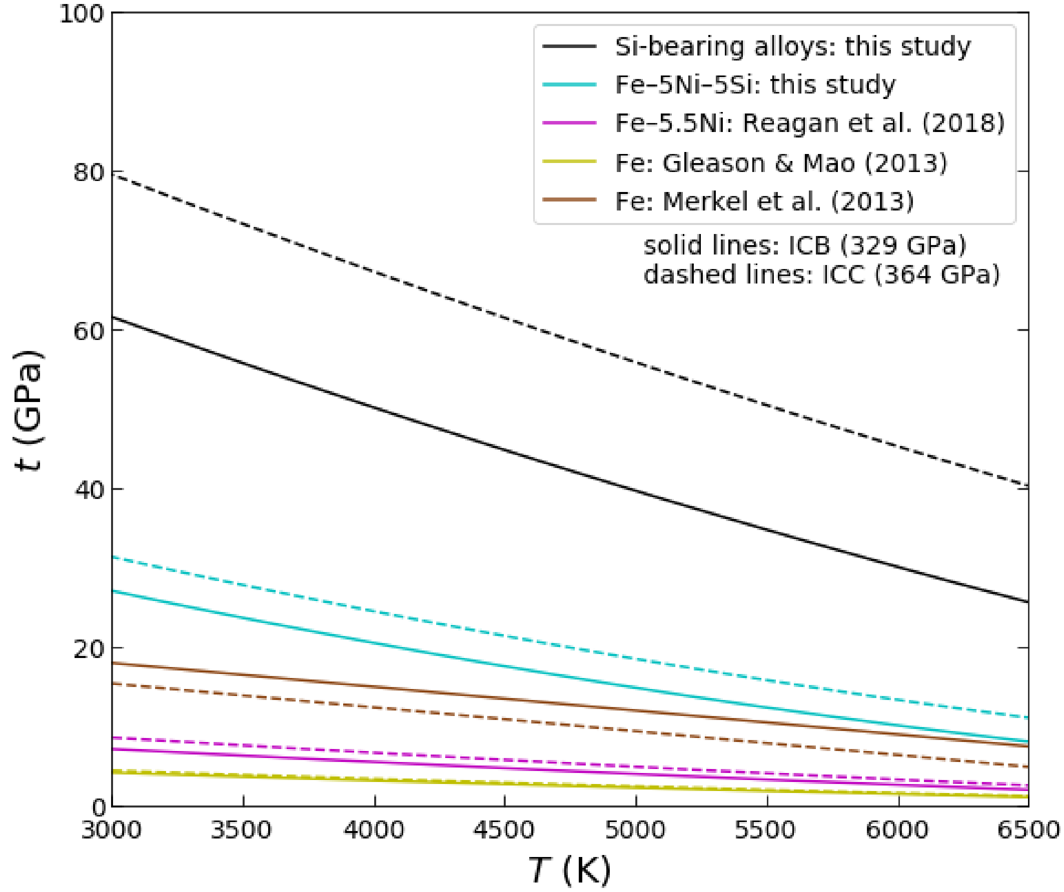

Alloy strength in the inner core as a function of temperature. Curves from Merkel et al. (2013) use that study's parametrization while those for other studies have been recalculated using Equation 6 and including ${}^{\partial Q}/_{\partial T}$. Curves from Reagan et al. (2018) assume that study's experimentally-determined strength ratio between Fe–5.5Ni and Fe–20Ni is constant with pressure and temperature. At inner core conditions, Si-bearing alloys are significantly stronger than alloys without light elements. The magnitude of this effect is reduced for the Fe–5Ni–5Si fit due to its smaller ${}^{\partial Q}/_{\partial P}$.

The enhanced strength of Si-bearing Fe alloys is well known in the bcc regime (e.g., Ros-Yanez et al., 2007) and attributed to the impedance of lattice dislocations by the presence of solute atoms (Labusch, 1970). This "solid-solution hardening" effect is enhanced for alloying elements with atomic radii dissimilar to the solvent, hence Fe–Ni alloys (where solute and solvent have nearly identical radii) shows little or no strengthening (e.g., Kotan et al., 2013). Solid solution hardening is known to occur in other hcp metals (e.g., Toda-Caraballo et al., 2015) and reduced dislocation mobility may influence hcp deformation mechanisms (e.g., Yoo et al., 2002), so both the strengths and textures of inner core alloys may be functions of their solutes' atomic radii.

**Figure 6.**

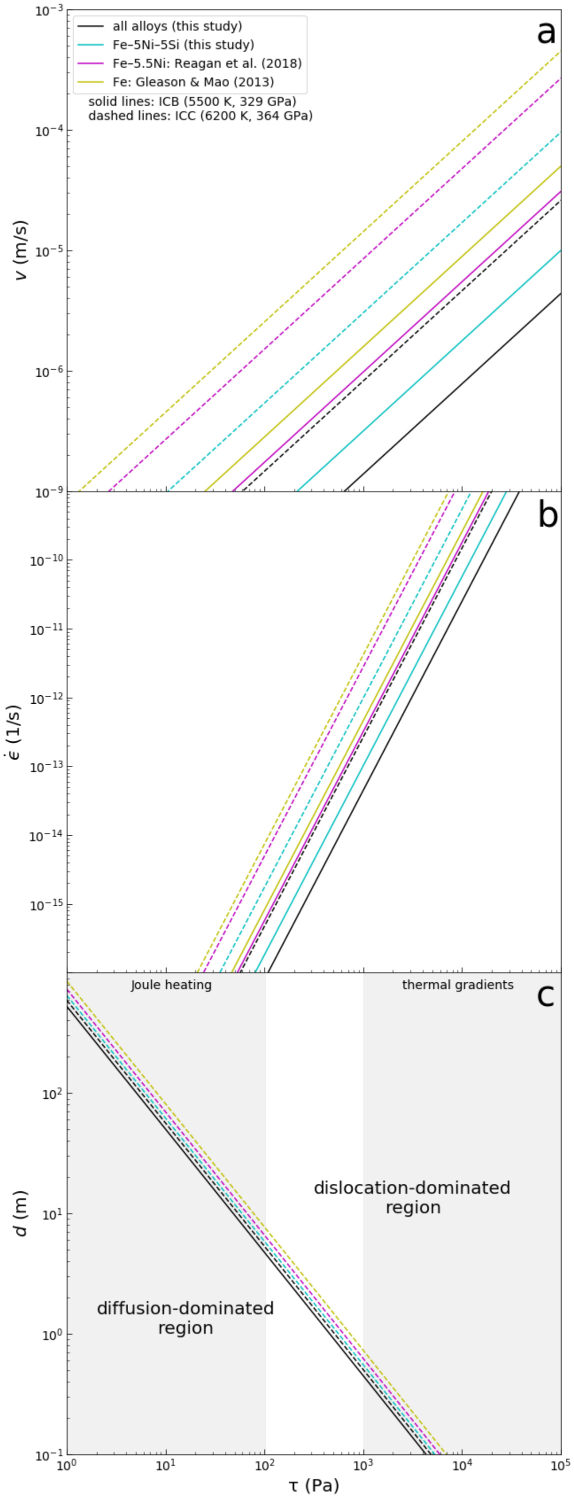

Dislocation velocity (**a**), strain rate (**b**), and critical grain size (**c**) as functions of differential stress τ. Equations and constants used are from Gleason & Mao (2013) and Reaman et al. (2011) and are listed in the Supporting Information. For clarity, only the “all alloys” ICB line is plotted in (**c**); the other ICB lines would be similarly offset from their corresponding ICC lines. The shaded “thermal gradients” (Jeanloz & Wenk, 1988) and “Joule heating” (Takehiro, 2011) regions are representative examples of proposed inner core stress ranges (see main text).

## 5 Conclusions

We investigated hcp Fe–Ni–Si alloy deformation textures and strengths with high-pressure radial X-ray diffraction experiments. These alloys plastically deform by the same principal mechanisms documented in other hcp metals, though possibly with greater pyramidal slip activity compared to pure ε-Fe at 300 K. Upon laser heating, we observed a change in the distribution of crystallographic preferred orientations which may suggest that basal slip is preferred at high temperatures. Experimental Fe–Ni–Si compositions are strong compared to previous Fe and Fe–Ni data and show significantly larger ${}^{\partial Q}/_{\partial P}$ values. Extrapolating to inner core conditions, Si-bearing alloys may be up to an order of magnitude stronger than pure Fe. This would reduce the mobility of anisotropy-favoring lattice dislocations by an equal factor. A mechanically strong inner core generally favors deformation by non-texturing diffusion creep and thus anisotropy as a crystallization (rather than a post-solidification) phenomenon. However, the large uncertainties on experimental and observational inner core parameters make it premature to conclude whether the strengthening effect of Si is significant in this regard.

## Acknowledgments

We thank Timothy Cavanaugh for performing the alloy EDS measurements, Martin Kunz and Andrew Doran for their assistance on beamline 12.2.2, Feng Lin for his experimental assistance, two anonymous reviewers for their valuable comments, and the editor for handling this manuscript. This work was funded in part by a National Science Foundation Graduate Research Fellowship awarded to M.C.B. (DGE1745303) and by a Henry Luce Foundation award to R.A.F. L.M. acknowledges support from the National Science Foundation through EAR-1654687. This work has been partially supported by the US Department of Energy National Nuclear Security Administration through the Capital-DOE Alliance Center which provided financial support for S.C. (DE-NA0003858). D.A. has received funding from the European Research Council (ERC) under the European Union's Horizon 2020 research and innovation program (grant agreement No. 724690). The Advanced Light Source is a Department of Energy Office of Science User Facility (contract no. DE-AC02-05CH11231). Beamline 12.2.2. is funded in part by the Consortium for Materials Properties Research in Earth Sciences (COMPRES) under NSF Cooperative Agreement EAR 10-43050. Part of this work was performed at the Harvard University Center for Nanoscale Systems, a member of the National Nanotechnology Coordinated Infrastructure Network, which is supported by the National Science Foundation (award no. 1541959). Supporting Information for this study, including values used to generate Figures 3–6, is available at https://doi.org/10.7910/DVN/QFE7CW.

## References

Alboussière, T., Deguen, R., & Melzani, M. (2010). Melting-induced stratification above the Earth's inner core due to convective translation. *Nature*, *466*(7307), 744–747. doi: 10.1038/nature09257

Anderson, O. L. (1965). Determination and Some Uses of Isotropic Elastic Constants of Polycrystalline Aggregates Using Single-Crystal Data. *Physical Acoustics*, *3*, 43–95. doi: 10.1016/B978-0-12-395669-9.50009-6

Antonangeli, D., Merkel, S., & Farber, D. L. (2006). Elastic anisotropy in hcp metals at high pressure and the sound wave anisotropy of the Earth's inner core. *Geophysical Research Letters*, *33*(24), L24303. doi: 10.1029/2006GL028237

Antonangeli, D., Morard, G., Paolasini, L., Garbarino, G., Murphy, C. A., Edmund, E., et al. (2018). Sound velocities and density measurements of solid hcp-Fe and hcp-Fe–Si (9 wt.%) alloy at high pressure: Constraints on the Si abundance in the Earth's inner core. *Earth and Planetary Science Letters*, *482*, 446–453. doi: 10.1016/j.epsl.2017.11.043

Aubert, J., Amit, H., Hulot, G., & Olson, P. (2008). Thermochemical flows couple the Earth's inner core growth to mantle heterogeneity. *Nature*, *454*(7205), 758–761. doi: 10.1038/nature07109

Bergman, M. I. (1997). Measurements of electric anisotropy due to solidification texturing and the implications for the Earth's inner core. *Nature*, *389*(6646), 60–63. doi: 10.1038/37962

Bergman, M. I. (1998). Estimates of the Earth's inner core grain size. *Geophysical Research Letters*, *25*(10), 1593–1596. doi: 10.1029/98GL01239

Bergman, M. I., Al-Khatatbeh, Y., Lewis, D. J., & Shannon, M. C. (2014). Deformation of directionally solidified alloys: Evidence for microstructural hardening of Earth's inner core? *Comptes Rendus - Geoscience*, *346*(5–6), 140–147. doi: 10.1016/j.crte.2014.04.004

Bergman, M. I., Giersch, L., Hinczewski, M., & Izzo, V. (2000). Elastic and attenuation anisotropy in directionally solidified (hcp) zinc, and the seismic anisotropy in the Earth's inner core. *Physics of the Earth and Planetary Interiors*, *117*, 139–151. doi: 10.1016/S0031-9201(99)00093-X

Bergman, M. I., Lewis, D. J., Myint, I. H., Slivka, L., Karato, S., & Abreu, A. (2010). Grain growth and loss of texture during annealing of alloys, and the translation of Earth's inner core. *Geophysical Research Letters*, *37*(22), L22313. doi: 10.1029/2010GL045103

Birch, F. (1964). Density and composition of mantle and core. *Journal of Geophysical Research*, *69*(20), 4377–4388. doi: 10.1029/jz069i020p04377

Birch, F. (1952). Elasticity and Constitution of the Earth's Interior. *Journal of Geophysical Research*, *57*(2), 227–286. doi: 10.1029/JZ057i002p00227

Buffett, B. A., & Wenk, H. R. (2001). Texturing of the earth's inner core by maxwell stresses. *Nature*, *413*(6851), 60–63. doi: 10.1038/35092543

Buffett, B. A. (2009). Onset and orientation of convection in the inner core. *Geophysical Journal International*, *179*(2), 711–719. doi: 10.1111/j.1365-246X.2009.04311.x

Chapuis, A., & Liu, Q. (2015). Simulations of texture evolution for HCP metals: Influence of the main slip systems. *Computational Materials Science*, *97*, 121–126. doi: 10.1016/j.commatsci.2014.10.017

Chateigner, D., Lutterotti, L., & Morales, M. (2019). Quantitative texture analysis and combined analysis. In *International Tables for Crystallography Volume H* (1st ed., pp. 555–580). International Union of Crystallography. doi: 10.1107/97809553602060000968

Creager, K. C. (1992). Anisotropy of the inner core from differential travel times of the phases PKP and PKIKP. *Nature*, *356*(6367), 309–314. doi: 10.1038/356309a0

Deguen, R., Alboussì Ere, T., & Cardin, P. (2013). Thermal convection in Earth’s inner core with phase change at its boundary. *Geophysical Journal International*, *194*, 1310–1334. doi: 10.1093/gji/ggt202

Deuss, A. (2014). Heterogeneity and Anisotropy of Earth’s Inner Core. *The Annual Review of Earth and Planetary Sciences*, *42*, 103–126. doi: 10.1146/annurev-earth-060313-054658

Dewaele, A., Loubeyre, P., Occelli, F., Mezouar, M., Dorogokupets, P. I., & Torrent, M. (2006). Quasihydrostatic equation of state of Iron above 2 Mbar. *Physical Review Letters*, *97*(21), 215504. doi: 10.1103/PhysRevLett.97.215504

Dubrovinsky, L. S., Dubrovinskaia, N. A., Saxena, S. K., Rekhi, S., & LeBihan, T. (2000). Aggregate shear moduli of iron up to 90 GPa and 1100 K. *Journal of Alloys and Compounds*, *297*(1–2), 156–161. doi: 10.1016/S0925-8388(99)00587-3

Durek, J. J., & Romanowicz, B. (1999). Inner core anisotropy inferred by direct inversion of normal mode spectra. *Geophysical Journal International*, *139*(3), 599–622. doi: 10.1046/j.1365-246X.1999.00961.x

Dziewonski, A. M., & Anderson, D. L. (1981). Preliminary Reference Earth Model. *Physics of the Earth and Planetary Interiors*, *25*, 297–356.

Edmund, E., Antonangeli, D., Decremps, F., Miozzi, F., Morard, G., Boulard, E., et al. (2019). Velocity-Density Systematics of Fe-5wt%Si: Constraints on Si Content in the Earth’s Inner Core. *Journal of Geophysical Research: Solid Earth*, *124*(4), 3436–3447. doi: 10.1029/2018JB016904

Edmund, E., Miozzi, F., Morard, G., Boulard, E., Clark, A., Decremps, F., et al. (2020). Axial Compressibility and Thermal Equation of State of hcp Fe–5wt% Ni–5wt% Si. *Minerals*, *10*(2), 98. doi: 10.3390/min10020098

Fan, H., Wang, Q., Tian, X., & El-Awady, J. A. (2017). Temperature effects on the mobility of pyramidal <c + a> dislocations in magnesium. *Scripta Materialia*, *127*, 68–71. doi: 10.1016/j.scriptamat.2016.09.002

Fei, Y., Ricolleau, A., Frank, M., Mibe, K., Shen, G., & Prakapenka, V. (2007). Toward an internally consistent pressure scale. *Proceedings of the National Academy of Sciences*, *104*(22), 9182–9186. doi: 10.1073/pnas.0609013104

Fischer, R. A., & Campbell, A. J. (2015). The axial ratio of hcp Fe and Fe-Ni-Si alloys to the conditions of Earth’s inner core. *American Mineralogist*, *100*(11–12), 2718–2724. doi: 10.2138/am-2015-5191

Fischer, R. A., Campbell, A. J., Reaman, D. M., Miller, N. A., Heinz, D. L., Dera, P., & Prakapenka, V. B. (2013). Phase relations in the Fe–FeSi system at high pressures and temperatures. *Earth and Planetary Science Letters*, *373*, 54–64. doi: 10.1016/j.epsl.2013.04.035

Fischer, R. A., Campbell, A. J., Caracas, R., Reaman, D. M., Heinz, D. L., Dera, P., & Prakapenka, V. B. (2014). Equations of state in the Fe-FeSi system at high pressures and temperatures. *Journal of Geophysical Research: Solid Earth*, *119*(4), 2810–2827. doi: 10.1002/2013JB010898

Fischer, R. A., Nakajima, Y., Campbell, A. J., Frost, D. J., Harries, D., Langenhorst, F., et al. (2015). High pressure metal-silicate partitioning of Ni, Co, V, Cr, Si, and O. *Geochimica et Cosmochimica Acta*, *167*, 177–194. doi: 10.1016/j.gca.2015.06.026

Georg, R. B., Halliday, A. N., Schauble, E. A., & Reynolds, B. C. (2007). Silicon in the Earth's core. *Nature*, *447*(7148), 1102–1106. doi: 10.1038/nature05927

Gleason, A. E., & Mao, W. L. (2013). Strength of iron at core pressures and evidence for a weak Earth's inner core. *Nature Geoscience*, *6*(7), 571–574. doi: 10.1038/ngeo1808

Hemley, R. J., Mao, H. K., Shen, G., Badro, J., Gillet, P., Hanfland, M., & Häusermann, D. (1997). X-ray imaging of stress and strain of diamond, iron, and tungsten at megabar pressures. *Science*, *276*(5316), 1242–1245. doi: 10.1126/science.276.5316.1242

Irving, J. C. E., & Deuss, A. (2011). Hemispherical structure in inner core velocity anisotropy. *Journal of Geophysical Research*, *116*(B4), B04307. doi: 10.1029/2010JB007942

Ishii, M., & Dziewoński, A. M. (2002). The innermost inner core of the earth: Evidence for a change in anisotropic behavior at the radius of about 300 km. *Proceedings of the National Academy of Sciences*, *99*(22), 14026–14030. doi: 10.1073/pnas.172508499

Jeanloz, R., & Wenk, H. -R. (1988). Convection and anisotropy of the inner core. *Geophysical Research Letters*, *15*(1), 72–75. doi: 10.1029/GL015i001p00072

Kanitpanyacharoen, W., Merkel, S., Miyagi, L., Kaercher, P., Tomé, C. N., Wang, Y., & Wenk, H. R. (2012). Significance of mechanical twinning in hexagonal metals at high pressure. *Acta Materialia*, *60*(1), 430–442. doi: 10.1016/j.actamat.2011.07.055

Karato, S. I. (1993). Inner core anisotropy due to the magnetic field-induced preferred orientation of iron. *Science*, *262*(5140), 1708–1711. doi: 10.1126/science.262.5140.1708

Karato, S. I. (2008). *Deformation of Earth Materials - An Introduction to the Rheology of Solid Earth* (1st ed.). Cambridge University Press.

Kassner, M. (2015). *Fundamentals of creep in metals and alloys* (3rd ed.). Elsevier Science.

Komabayashi, T., Pesce, G., Morard, G., Antonangeli, D., Sinmyo, R., & Mezouar, M. (2019). Phase transition boundary between fcc and hcp structures in Fe-Si alloy and its implications for terrestrial planetary cores. *American Mineralogist*, *104*(1), 94–99. doi: 10.2138/am-2019-6636

Koot, L., & Dumberry, M. (2011). Viscosity of the Earth's inner core: Constraints from nutation observations. *Earth and Planetary Science Letters*, *308*(3–4), 343–349. doi: 10.1016/j.epsl.2011.06.004

Kotan, H., Darling, K. A., Saber, M., Scattergood, R. O., & Koch, C. C. (2013). An in situ experimental study of grain growth in a nanocrystalline $Fe_{91}Ni_{8}Zr_{1}$ alloy. *Journal of Materials Science*, *48*(5), 2251–2257. doi: 10.1007/s10853-012-7002-1

Kunz, M., MacDowell, A. A., Caldwell, W. A., Cambie, D., Celestre, R. S., Domning, E. E., et al. (2005). A beamline for high-pressure studies at the Advanced Light Source with a superconducting bending magnet as the source. *Journal of Synchrotron Radiation*, 12, 650–658). doi: 10.1107/S0909049505020959

Kunz, M., Yan, J., Cornell, E., Domning, E. E., Yen, C. E., Doran, A., et al. (2018). Implementation and application of the peak scaling method for temperature measurement in the laser heated diamond anvil cell. *Review of Scientific Instruments*, *89*(8), 083903. doi: 10.1063/1.5028276

Kuwayama, Y., Sawai, T., Hirose, K., Sata, N., & Ohishi, Y. (2009). Phase relations of iron-silicon alloys at high pressure and high temperature. *Physics and Chemistry of Minerals*, *36*(9), 511–518. doi: 10.1007/s00269-009-0296-0

Labusch, R. (1970). A Statistical Theory of Solid Solution Hardening. *Physica Status Solidi (B)*, *41*(2), 659–669. doi: 10.1002/pssb.19700410221

Lasbleis, M., & Deguen, R. (2014). Building a regime diagram for the Earth's inner core. *Physics of the Earth and Planetary Interiors*, *247*, 80–93. doi: 10.1016/j.pepi.2015.02.001

Ledbetter, H. M., & Reed, R. P. (1973). Elastic Properties of Metals and Alloys, I. Iron, Nickel, and Iron-Nickel Alloys. *Journal of Physical and Chemical Reference Data*, *2*(3), 531–618. doi: 10.1063/1.3253127

Lehmann, I. (1936). P'. *Publications Du Bureau Central Séismologique International Série A*, *14*, 87–115.

Lin, J.-F. (2003). Sound velocities of iron-nickel and iron-silicon alloys at high pressures. *Geophysical Research Letters*, *30*(21), 2112. doi: 10.1029/2003GL018405

Lincot, A., Cardin, P., Deguen, R., & Merkel, S. (2016). Multiscale model of global inner-core anisotropy induced by hcp alloy plasticity. *Geophysical Research Letters*, *43*(3), 1084–1091. doi: 10.1002/2015GL067019

Lincot, A., Deguen, R., Merkel, S., & Cardin, P. (2014). Seismic response and anisotropy of a model hcp iron inner core. *Comptes Rendus - Geoscience*, *346*(5–6), 148–157. doi: 10.1016/j.crte.2014.04.001

Liu, J., Lin, J., Alatas, A., Hu, M. Y., Zhao, J., & Dubrovinsky, L. (2016). Seismic parameters of hcp-Fe alloyed with Ni and Si in the Earth's inner core. *Journal of Geophysical Research: Solid Earth*, *121*(2), 610–623. doi: 10.1002/2015JB012625

Lutterotti, L., Matthies, S., & Wenk, H. R. (1999). MAUD (material analysis using diffraction): a user friendly Java program for Rietveld texture analysis and more. *Proceedings of the Twelfth International Conference on Textures of Materials*, *1*, 1599.

Mao, H. K., Shu, J., Shen, G., Hemley, R. J., Li, B., & Singh, A. K. (1999). Erratum: Elasticity and rheology of iron above 220 GPa and the nature of the Earth's inner core (Nature (1998) 396 (741-743)). *Nature*, *399*(6733), 280. doi: 10.1038/20472

Mao, Z., Lin, J. F., Liu, J., Alatas, A., Gao, L., Zhao, J., & Mao, H. K. (2012). Sound velocities of Fe and Fe-Si alloy in the Earth's core. *Proceedings of the National Academy of Sciences*, *109*(26), 10239–10244. doi: 10.1073/pnas.1207086109

Mccusker, L. B., Von Dreele, R. B., Cox, D. E., Louër, D., & Scardi, P. (1999). Rietveld refinement guidelines. *Journal of Applied Crystallography*, *32*(1), 36–50. doi: 10.1107/S0021889898009856

McDonough, W. F., & Sun, S. s. (1995). The composition of the Earth. *Chemical Geology*, *120*(3–4), 223–253. doi: 10.1016/0009-2541(94)00140-4

Merkel, S., Liermann, H. P., Miyagi, L., & Wenk, H. R. (2013). In situ radial X-ray diffraction study of texture and stress during phase transformations in bcc-, fcc-and hcp-iron up to 36 GPa and 1000 K. *Acta Materialia*, *61*(14), 5144–5151. doi: 10.1016/j.actamat.2013.04.068

Merkel, S., Gruson, M., Wang, Y., Nishiyama, N., & Tomé, C. N. (2012). Texture and elastic strains in hcp-iron plastically deformed up to 17.5 GPa and 600 K: experiment and model. *Modelling and Simulation in Materials Science and Engineering*, *20*(2), 024005. doi: 10.1088/0965-0393/20/2/024005

Merkel, S., Wenk, H. R., Gillet, P., Mao, H. kwang, & Hemley, R. J. (2004). Deformation of polycrystalline iron up to 30GPa and 1000K. *Physics of the Earth and Planetary Interiors*, *145*(1–4), 239–251. doi: 10.1016/j.pepi.2004.04.001

Merkel, S., & Yagi, T. (2005). X-ray transparent gasket for diamond anvil cell high pressure experiments. *Review of Scientific Instruments*, *76*(4), 046109. doi: 10.1063/1.1884195

Miyagi, L., Kunz, M., Knight, J., Nasiatka, J., Voltolini, M., & Wenk, H. R. (2008). In situ phase transformation and deformation of iron at high pressure and temperature. *Journal of Applied Physics*, *104*(10), 1–9. doi: 10.1063/1.3008035

Monnereau, M., Calvet, M., Margerin, L., & Souriau, A. (2010). Lopsided growth of Earth's inner core. *Science*, *328*(5981), 1014–1017. doi: 10.1126/science.1186212

Morard, G., Andrault, D., Guignot, N., Siebert, J., Garbarino, G., & Antonangeli, D. (2011). Melting of Fe-Ni-Si and Fe-Ni-S alloys at megabar pressures: implications for the core-mantle boundary temperature. *Physics and Chemistry of Minerals*, *38*(10), 767–776. doi: 10.1007/s00269-011-0449-9

Morrison, R. A., Jackson, J. M., Sturhahn, W., Zhao, J., & Toellner, T. S. (2019). High pressure thermoelasticity and sound velocities of Fe-Ni-Si alloys. *Physics of the Earth and Planetary Interiors*, *294*, 106268. doi: 10.1016/j.pepi.2019.05.011

Nishihara, Y., Ohuchi, T., Kawazoe, T., Seto, Y., Maruyama, G., Higo, Y., et al. (2018). Deformation-induced crystallographic-preferred orientation of hcp-iron: An experimental study using a deformation-DIA apparatus. *Earth and Planetary Science Letters*, *490*, 151–160. doi: 10.1016/j.epsl.2018.03.029

Ozawa, H., Hirose, K., Yonemitsu, K., & Ohishi, Y. (2016). High-pressure melting experiments on Fe–Si alloys and implications for silicon as a light element in the core. *Earth and Planetary Science Letters*, *456*, 47–54. doi:10.1016/j.epsl.2016.08.042

Ouzounis, A., & Creager, K. C. (2001). Isotropy overlying anisotropy at the top of the inner core. *Geophysical Research Letters*, *28*(22), 4331–4334. doi: 10.1029/2001GL013341

Poirier, J. P., & Langenhorst, F. (2002). TEM study of an analogue of the Earth's inner core ε-Fe. *Physics of the Earth and Planetary Interiors*, *129*(3–4), 347–358. doi: 10.1016/S0031-9201(01)00300-4

Prescher, C., & Prakapenka, V. B. (2015). DIOPTAS: A program for reduction of two-dimensional X-ray diffraction data and data exploration. *High Pressure Research*, *35*(3), 223–230. doi: 10.1080/08957959.2015.1059835

Reagan, M. M., Gleason, A. E., Liu, J., Krawczynski, M. J., Van Orman, J. A., & Mao, W. L. (2018). The effect of nickel on the strength of iron nickel alloys: Implications for the Earth's inner core. *Physics of the Earth and Planetary Interiors*, *283*, 43–47. doi: 10.1016/j.pepi.2018.08.003

Reaman, D. M., Daehn, G. S., & Panero, W. R. (2011). Predictive mechanism for anisotropy development in the Earth's inner core. *Earth and Planetary Science Letters*, *312*(3–4), 437–442. doi: 10.1016/j.epsl.2011.10.038

Ringwood, A. E. (1961). Silicon in the metal phase of enstatite chondrites and some geochemical implications. *Geochimica et Cosmochimica Acta*, *25*(1), 1–13. doi: 10.1016/0016-7037(61)90056-4

Ros-Yanez, T., Ruiz, D., Barros, J., Houbaert, Y., & Colás, R. (2007). Study of deformation and aging behaviour of iron-silicon alloys. *Materials Science and Engineering A*, *447*(1–2), 27–34. doi: 10.1016/j.msea.2006.10.075

Sakai, T., Ohtani, E., Hirao, N., & Ohishi, Y. (2011). Stability field of the hcp-structure for Fe, Fe-Ni, and Fe-Ni-Si alloys up to 3 Mbar. *Geophysical Research Letters*, *38*(9), L09302. doi: 10.1029/2011GL047178

Sakairi, T., Sakamaki, T., Ohtani, E., Fukui, H., Kamada, S., Tsutsui, S., et al. (2018). Sound velocity measurements of hcp Fe-Si alloy at high pressure and high temperature by inelastic X-ray scattering. *American Mineralogist*, *103*(1), 85–90. doi: 10.2138/am-2018-6072

Sayers, C. M. (1989). Seismic anisotropy of the inner core. *Geophysical Research Letters*, *16*(3), 267–270. doi: 10.1029/GL016i003p00267

Siebert, J., Badro, J., Antonangeli, D., Ryerson, F. J. (2013). Terrestrial accretion under oxidizing conditions. *Science,* 339, 1194–1197. doi: 10.1126/science.1227923.

Singh, A. K., Balasingh, C., Mao, H. K., Hemley, R. J., & Shu, J. (1998). Analysis of lattice strains measured under nonhydrostatic pressure. *Journal of Applied Physics*, *83*(12), 7567–7575. doi: 10.1063/1.367872

Speziale, S., Zha, C.-S., Duffy, T. S., Hemley, R. J., & Mao, H. (2001). Quasi-hydrostatic compression of magnesium oxide to 52 GPa: Implications for the pressure-volume-temperature equation of state. *Journal of Geophysical Research: Solid Earth*, *106*(B1), 515–528. doi: 10.1029/2000jb900318

Steinberg, D. J., Cochran, S. G., & Guinan, M. W. (1980). A constitutive model for metals applicable at high-strain rate. *Journal of Applied Physics*, *51*(3), 1498–1504. doi: 10.1063/1.327799

Steinle-Neumann, G., Stixrude, L., Cohen, R. E., & Gülseren, O. (2001). Elasticity of iron at the temperature of the Earth's inner core. *Nature*, *413*(6851), 57–60. doi:10.1038/35092536

Stixrude, L., & Cohen, R. E. (1995). High-pressure elasticity of iron and anisotropy of earth's inner core. *Science*, *267*(5206), 1972–1975. doi: 10.1126/science.267.5206.1972

Su, W., & Dziewonski, A. M. (1995). Inner core anisotropy in three dimensions. *Journal of Geophysical Research: Solid Earth*, *100*(B6), 9831–9852. doi: 10.1029/95JB00746

Takehiro, S. I. (2011). Fluid motions induced by horizontally heterogeneous Joule heating in the Earth's inner core. *Physics of the Earth and Planetary Interiors*, *184*(3–4), 134–142. doi: 10.1016/j.pepi.2010.11.002

Tateno, S., Hirose, K., Ohishi, Y., & Tatsumi, Y. (2010). The structure of iron in earth's inner core. *Science*, *330*(6002), 359–361. doi: 10.1126/science.1194662

Tateno, S., Hirose, K., Komabayashi, T., Ozawa, H., & Ohishi, Y. (2012). The structure of Fe-Ni alloy in Earth's inner core. *Geophysical Research Letters*, *39*(12), L12305. doi: 10.1029/2012GL052103

Tateno, S., Kuwayama, Y., Hirose, K., & Ohishi, Y. (2015). The structure of Fe-Si alloy in Earth's inner core. *Earth and Planetary Science Letters*, *418*, 11–19. doi: 10.1016/j.epsl.2015.02.008

Toda-Caraballo, I., & Rivera-Díaz-Del-Castillo, P. E. J. (2015). Modelling solid solution hardening in high entropy alloys. *Acta Materialia*, *85*, 14–23. doi: 10.1016/j.actamat.2014.11.014

Van Orman, J. A. (2004). On the viscosity and creep mechanism of Earth's inner core. *Geophysical Research Letters*, *31*(20), L20606. doi: 10.1029/2004GL021209

Vočadlo, L., Dobson, D. P., & Wood, I. G. (2009). Ab initio calculations of the elasticity of hcp-Fe as a function of temperature at inner-core pressure. *Earth and Planetary Science Letters*, *288*(3–4), 534–538. doi: 10.1016/j.epsl.2009.10.015

Wenk, H. R., Matthies, S., Donovan, J., & Chateigner, D. (1998). BEARTEX: A Windows-based program system for quantitative texture analysis. *Journal of Applied Crystallography*, *31*(2), 262–269. doi: 10.1107/S002188989700811X

Wenk, H. R., Matthies, S., Hemley, R. J., Mao, H. K., & Shu, J. (2000). The plastic deformation of iron at pressures of the Earth's inner core. *Nature*, *405*(6790), 1044–1047. doi: 10.1038/35016558

Yamazaki, D., Tsujino, N., Yoneda, A., Ito, E., Yoshino, T., Tange, Y., & Higo, Y. (2017). Grain growth of ε-iron: Implications to grain size and its evolution in the Earth's inner core. *Earth and Planetary Science Letters*, *459*, 238–243. doi: 10.1016/j.epsl.2016.11.049

Yoo, M. H., Morris, J. R., Ho, K. M., & Agnew, S. R. (2002). Nonbasal deformation modes of HCP metals and alloys: Role of dislocation source and mobility. *Metallurgical and Materials Transactions A: Physical Metallurgy and Materials Science*, *33*(3), 813–822. doi: 10.1007/s11661-002-0150-1

Yoshida, S., Sumita, I., & Kumazawa, M. (1996). Growth model of the inner core coupled with the outer core dynamics and the resulting elastic anisotropy. *Journal of Geophysical Research: Solid Earth*, *101*(B12), 28085–28103. doi: 10.1029/96jb02700